















# Experimental Scattering Matrices of Martian Dust Aerosols with Narrow Particle-size Distributions

Julia Martikainen<sup>1,2</sup> , Olga Muñoz<sup>1</sup> , Juan Carlos Gómez Martín<sup>1</sup> , Teresa Jardiel<sup>3</sup> , Marco Peiteado<sup>3</sup> , Amador C. Caballero<sup>3</sup> , Santiago Pérez-Hoyos<sup>4</sup> , Agustín Sánchez Lavega<sup>4</sup> , Tim Becker<sup>5</sup> , Gerhard Wurm<sup>5</sup> ,

Yannick Willame<sup>6</sup> , and Ann Carine Vandaele<sup>6</sup> 

<sup>1</sup> Instituto de Astrofísica de Andalucía, CSIC, Granada, Spain

<sup>2</sup> University of Helsinki, Department of Physics, Helsinki, Finland

<sup>3</sup> Instituto de Cerámica y Vidrio, CSIC, Madrid, Spain

<sup>4</sup> Departamento de Física Aplicada I, Escuela de Ingeniería de Bilbao, Universidad del País Vasco (UPV/EHU), Bilbao, Spain

<sup>5</sup> University of Duisburg-Essen, Faculty of Physics, Duisburg, Germany

<sup>6</sup> Belgian Institute for Space Aeronomy (IASB-BIRA), Brussels, Belgium

Received 2024 March 11; revised 2024 May 10; accepted 2024 June 10; published 2024 July 29

## Abstract

We present experimental scattering matrices of the JSC Mars-1, MMS-2, and MGS-1 simulants at 488 and 640 nm. The analogs were processed so that narrow size distributions representative of Martian dust aerosols during different dust cycles were obtained. We find that the forward peak of the phase function depends on particle size as it becomes narrower with increasing size, whereas the side- and backscattering directions depend on both composition and size so that increasing size and decreasing absorption produce a flatter curve. The position and maximum of the degree of linear polarization varies based on particle size and composition, and the negative polarization branch is more prominent for wavelength-scale particles diminishing with increasing size. The linear depolarization is strongly affected by size and composition. Finally, we compare sky-brightness curves measured by the Navcam and Hazcam engineering cameras on board the Mars Science Laboratory rover to the measured phase functions. The observations show a narrower peak at the forward direction and a flatter curve toward the side- and backscattering directions with an increasing dust load in the atmosphere, similar to what can be seen for the measured phase functions of the analogs with increasing particle size. In the case of the analogs, the flattening of the curve can be caused by an increase in multiple scattering within a particle by wavelength-scale surface roughness and/or internal inclusions. For the observed sky brightnesses, particle aggregation and multiple scattering among particles in denser dust conditions play a major role.

*Unified Astronomy Thesaurus concepts:* Mars (1007); Experimental data (2371); Polarimetry (1278)

## 1. Introduction

This experimental study is motivated by the lack of satisfactory modeling approaches traditionally used to mimic the role of dust particles in the Martian radiative budget. Airborne dust particles scatter and absorb solar radiation, thereby playing a key role in determining the thermal structure of the Martian atmosphere. The net radiative impact of mineral dust particles in the atmosphere constitutes one of the major uncertainties in Martian atmospheric studies (Haberle et al. 2017). At the root of this problem lies a lack of understanding of how solar radiation is scattered in all directions after interacting with a cloud of particles, i.e., a lack of accurate dust/cloud scattering properties. Modeling scattering properties is straightforward for homogeneous spheres but is extremely challenging for irregular dust particles. As shown by the Phoenix Lander microscope images (Smith et al. 2009), Martian dust particles are shown to have a wide variety of shapes and sizes. However, the scattering function of Martian dust particles is often derived by assuming simplified particle shapes, such as spheres or spheroids (see e.g., Modak et al. 2019; Chen-Chen et al. 2021). This approach is highly unrealistic as shown by previous laboratory measurements

(Dabrowska et al. 2015). This is well known for the Earth's atmosphere due to numerous studies of ice clouds and solid aerosols (see e.g., Nousiainen 2009). It has been proven that the use of the scattering model for too-simplistic particle shapes in the case of irregular mineral dust can lead to significant errors in the retrieved optical thickness (Mishchenko et al. 2003).

Numerical scattering simulations are limited to certain size ranges and simplified model particles (Min et al. 2003; Moreno et al. 2007; Zubko et al. 2013; Escobar-Cerezo et al. 2017). The exact solution for realistic polydispersions of irregular dust particles covering all sizes and shapes we can find in the Martian atmosphere remains an extremely difficult problem. Consequently, experimental studies of light scattering by ensembles of dust particles covering different size ranges and compositions are a key tool to interpret space observations. Preliminary measurements for Martian dust analogs performed at the IAA Cosmic Dust Laboratory (CODULAB) show that taking into account the irregular shape of the particles is mandatory for a correct interpretation of observational data (Dabrowska et al. 2015).

The current knowledge of the Martian atmosphere is limited by a lack of global measurements of aerosols and winds. The dust and CO<sub>2</sub> cycles are partially linked and their effects on the atmospheric circulation change the global wind field. Therefore, simultaneously measuring the height-resolved wind and dust profiles is important for new Mars missions (Cremons et al. 2020). Lidar instruments can provide accurate measurements of



Original content from this work may be used under the terms of the [Creative Commons Attribution 4.0 licence](https://creativecommons.org/licenses/by/4.0/). Any further distribution of this work must maintain attribution to the author(s) and the title of the work, journal citation and DOI.

winds, temperatures, densities, and aerosols (Amzajerdian et al. 2012). In 2008, the lidar instrument on the Phoenix mission (Whiteway et al. 2008) operated nearly daily in order to observe backscattering from dust and water-ice clouds (Whiteway et al. 2009). The new MARLI lidar is being designed to provide global, height-resolved measurements of line-of-sight winds, aerosol backscatter, and the depolarization ratio (Cremons et al. 2020). Backscattered light and the depolarization ratio are directly linked to the scattering matrix, and thus studying scattering matrices of Martian dust analogs in Earth-based laboratories provides insight into lidar observations.

In this paper, the scattering matrices of three well-characterized Martian dust simulants have been obtained for three narrow particle-size distributions. These simulants have been chosen from a range of representative dust analogs discussed in the recent literature. The bulk chemical composition and mineralogy have been retrieved from the sample manufacturers and the relevant literature and double checked in our facilities. Knowledge of the physical properties of the samples is critical to ensure that they are relevant as Martian dust simulants. Moreover, the physical properties that determine how dust particles scatter light (chemical composition, size distribution, morphology, refractive indices) are needed to model the scattering matrices using electromagnetic scattering codes and to perform radiative-transfer calculations.

Taking into account the full scattering matrix in numerical simulations is crucial as it has been shown (Moreno et al. 2002; Stam & Hovenier 2005) that neglecting the polarized nature of light not only leads to significant errors in the determination of the scattered contribution to the measured flux, but it also introduces errors (which are wavelength dependent) into the atmospheric optical thickness, impacting the gaseous mixing ratio (i.e., abundances) obtained from these spectra. Stam & Hovenier (2005) found that neglecting polarization when deriving the methane-mixing ratio from simulated reflected spectra of a giant planet led to values larger by tens of percent.

The paper is organized as follows. In Section 2 we present the experimental apparatus and scattering-matrix formalism. Sample characterization is described in Section 3, whereas the experimental data is presented in Section 4. In Section 5, we analyze the measured data, and in Section 6 compare the measurements to the sky-brightness curves observed by the Navcam and Hazcam engineering cameras on board the Mars Science Laboratory rover. Finally, the study is summarized in Section 7.

## 2. Experimental Apparatus and Scattering-matrix Formalism

Experimental scattering matrices presented in this work have been obtained at the CODULAB located at the Instituto de Astrofísica de Andalucía in Granada, Spain. The experimental apparatus is described in Muñoz et al. (2010, 2011). In this work, we use two diode fiber-pigtail lasers that emit at 488 and 640 nm. The experimental data span over a scattering-angle range from  $3^\circ$  to  $177^\circ$ . Briefly, we combine electro-optic modulation with lock-in detection for the concurrent determination of several elements of the  $4 \times 4$  scattering matrix,  $\mathbf{F}$  (Hovenier et al. 2004). The modulated laser beam is scattered by the cloud of randomly oriented dust particles located in a jet stream produced by an aerosol generator.

The elements  $F_{ij}$  of the scattering matrix depend on the wavelength ( $\lambda$ ) on the incident beam, the direction of the

scattered beam and on the physical properties of the scattering particles (size, morphology, and refractive index). The direction of scattering is defined by the angle between the directions of propagation of the incident and scattering beams. At CODULAB we deal with clouds of randomly oriented particles located in a turbulent jet stream produced by an aerosol generator. Further, the amount of particles in the scattering volume is high enough for safely assuming mirror symmetry. Under those conditions the scattering matrix contains six nonvanishing elements and the scattering direction is fully described by means of the scattering angle ( $\theta$ ) as described in Hovenier et al. (2004), Section 2.4.

For unpolarized incident light, the first element of the scattering matrix,  $F_{11}(\theta)$ , is proportional to the flux of the scattered light and is called the phase function here. Moreover, the  $-(F_{12}(\theta)/F_{11}(\theta))$  ratio equals the degree of linear polarization ( $P$ ). Similarly, if the incident beam is 100% linearly polarized parallel to the scattering plane the linear depolarization ratio  $\delta_L$  can be defined in terms of the scattering-matrix elements (see e.g., Mishchenko & Hovenier 1995; Muñoz et al. 2021):

$$\delta_L(\theta) = \frac{1 - F_{22}(\theta)/F_{11}(\theta)}{1 + 2F_{12}(\theta)/F_{11}(\theta) + F_{22}(\theta)/F_{11}(\theta)}. \quad (1)$$

In the case of a cloud consisting of spherical particles the  $F_{22}/F_{11}$  ratio equals unity at all phase angles. The linear depolarization ratio is commonly used in lidar atmospheric measurements to characterize aerosol particle shapes, sizes, and chemical compositions. For randomly oriented particles with mirror symmetry the scattering matrix has only six independent nonzero elements:  $F_{11}$ ,  $F_{12}$ ,  $F_{22}$ ,  $F_{33}$ ,  $F_{34}$ , and  $F_{44}$  (Mishchenko et al. 2002). In this work we present the measured  $F_{11}(\theta)$ ,  $-F_{12}(\theta)/F_{11}(\theta)$ ,  $F_{22}(\theta)/F_{11}(\theta)$ ,  $F_{33}(\theta)/F_{11}(\theta)$ ,  $F_{34}(\theta)/F_{11}(\theta)$ , and  $F_{44}(\theta)/F_{11}(\theta)$  of our set of Martian dust analogs. The measured  $F_{11}$  element is normalized to 1 at  $30^\circ$ .

## 3. The Martian Dust Analogs

### 3.1. Composition

We selected three compositionally and spectrally distinctive Martian dust analogs (see Figure 1). The JSC Mars-1 sample, where JSC stands for Johnson Space Center, is a spectral simulant developed by JSC that replicates the visible/near-infrared reflectance properties of dust-covered terrains on Mars. It was sourced from palagonitic tephra from the Pu'u Nene cinder cone in Hawaii (Allen et al. 1998). The first set of samples used in this work have been obtained directly from JSC. There are already scattering matrices of this material in the Granada–Amsterdam light-scattering database (Dabrowska et al. 2015), although the size distribution of these samples (fraction with radius  $r < 100 \mu\text{m}$ ) does not conform with the size distribution of airborne Martian dust inferred from occultation remote-sensing observations (Fedorova et al. 2014) and ground-rover observations (Lemmon et al. 2015), having a much broader size distribution. It has been shown that the JSC Mars-1 simulant contains a higher level of  $\text{H}_2\text{O}$  and OH than Martian dust (Allen et al. 1998). However, heating the samples to remove the volatile component did not have any significant impact on the scattering properties (Dabrowska et al. 2015).

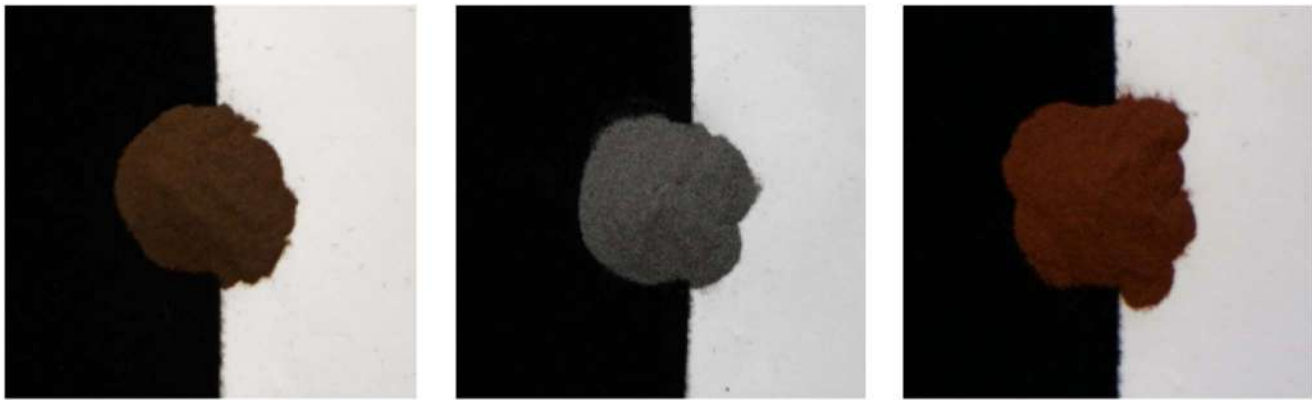


**Figure 1.** The L size fractions of the JSC Mars-1 (left), MGS-1 (middle), and MMS-2 (right) analogs.

The bulk element chemistry of the three dust simulants is listed in Table 1. Table 2 lists the mineralogy of the samples. This table contains both qualitative and semiquantitative X-ray diffraction (XRD) information. In the case of JSC Mars-1, the major constituent is palagonite, which is a heterogeneous mixture of minerals that is poorly defined. Crystalline and amorphous phases that appear together in composite particles are not normally present as discrete single-phase particles. The Mars Global Simulant (MGS-1) is a mineralogical standard for basaltic soils on Mars, developed based on quantitative mineralogy from the Mars Science Laboratory (MSL) Curiosity rover. It is made by sourcing individual minerals, including a proper treatment of the X-ray amorphous component (Cannon et al. 2019). Therefore, the mineralogy of MGS-1 is well known and provided by the manufacturer. The Mojave Mars Simulant (MMS) was developed as a geotechnical Mars simulant by the Jet Propulsion Laboratory (JPL). It was sourced from a basaltic flow in the Mojave Desert (Peters et al. 2008). The Martian Garden<sup>7</sup> is a company that sells two Mars simulants, MMS-1 and MMS-2. They claim these are the same as the MMS produced by JPL. The Martian Garden company had no contact with the developers of the original MMS simulant, but is mining material from the same general region. MMS-2, the “Enhanced Mars Simulant,” is spiked with “Iron III Oxide, Magnesium Oxide, Sulfates and Silicates” to make up for discrepancies in bulk chemistry between Mars and MMS-1. The XRD analysis of the MMS-2 sample is roughly consistent with the information in the existing literature (see Kemmerer 2019).

### 3.2. Size Distributions

In this work, we used three narrow size distributions spanning over a broad scattering-size range. These narrow size distributions enable us to study the effect of size on the light-scattering behavior of the materials.

All of the narrow size distributions were obtained at Instituto de Cerámica y Vidrio through an intricate process. First, the bulk powder was lightly milled to ensure a homogeneous phase distribution, as we observed that sieving without previous milling can occasionally lead to compositional deviations (particularly in the case of the MMS-2 sample). Milling times from 5 to 15 minutes were then applied for the different analogs, these being adjusted independently until a similar particle-size distribution was obtained in all cases. The milled powders were

<sup>7</sup> <https://www.themartiangarden.com>

**Table 1**

Volatile-free, Normalized Bulk Major Chemistry (%wt) of the Martian Dust Simulants Used in this Work

Oxide	JSC Mars-1 <sup>a</sup>	MGS-1 <sup>b</sup>	MMS-2 <sup>c</sup>
SiO <sub>2</sub>	43.5	44.2	43.8
TiO <sub>2</sub>	3.8	0.6	0.8
Al <sub>2</sub> O <sub>3</sub>	23.3	13.2	13.1
Cr <sub>2</sub> O <sub>3</sub>	...	...	<0.1
FeO <sub>T</sub>	15.6	11.5	18.4
MnO	0.3	0.1	0.1
CaO	6.2	7.6	8.0
MgO	3.4	15.0	6.7
Na <sub>2</sub> O	2.4	1.5	2.5
K <sub>2</sub> O	0.6	0.6	0.4
P <sub>2</sub> O <sub>5</sub>	0.9	0.1	0.1
SO <sub>3</sub>	...	...	6.1
Lost in ignition	...	5.5	...

**Notes.**

<sup>a</sup> From Allen et al. (1998).

<sup>b</sup> As specified by the supplier company Exolith Lab. The total excludes trace elements.

<sup>c</sup> From the elemental composition provided by the supplier company The Martian Garden.

then dry sieved using a 40  $\mu\text{m}$  mesh. Next, in order to favor the dispersion of the particles and “loosen” the smaller (stuck) ones, a surfactant (0.3 wt% Dolapix CE64, Zschimmer & Schwarz) was added to the sieved powders that were then ultrasonicated and sieved through a 20  $\mu\text{m}$  mesh in an alcoholic medium. As a result, the smaller particles passed the 20  $\mu\text{m}$  sieve, leaving a dust fraction with a narrow distribution in the range of  $7 < d < 40 \mu\text{m}$  (L fraction). The preparation of the M and S fractions starts from the powders previously wet sieved through a 20  $\mu\text{m}$  mesh. These were again dispersed in alcoholic medium in an ultrasonic bath and then wet sieved using a 5  $\mu\text{m}$  mesh. With this approach, practically all particles larger than 10  $\mu\text{m}$  in diameter were successfully removed. After this procedure, the powders below 5  $\mu\text{m}$  were again sonicated in an ultrasonic bath and centrifuged to separate the particles into two fractions: one centered at 3–4  $\mu\text{m}$  in diameter (sediment), and other containing submicron particles (supernatant).

The final size distribution measurements were carried out at Instituto de Cerámica y Vidrio using a laser light-scattering particle sizer (Malvern Mastersizer 3000).

All of the measured particle-size distributions are shown in Figure 2. The particle sizer provides the distribution of surface-

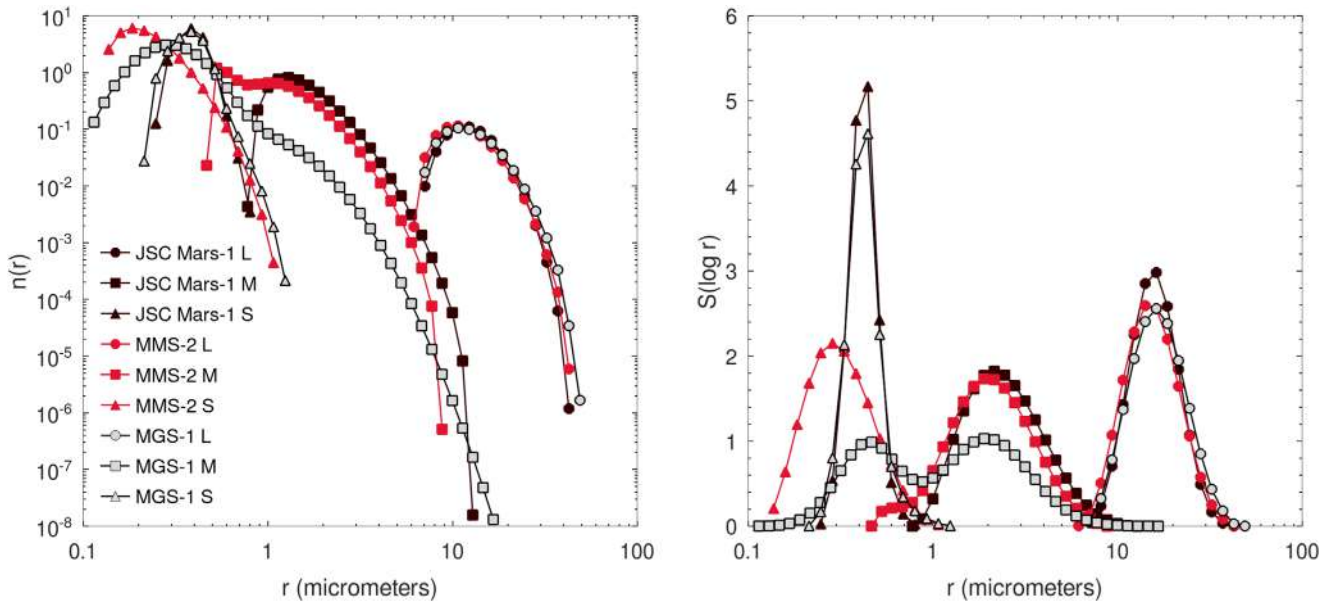


**Figure 2.** Number distributions (left) and projected surface area distributions (right) of the JSC Mars-1, MGS-1, and MMS-2 S, M, and L size fractions.

**Table 2**  
Mineralogy (%wt) of the Martian Dust Simulants

	JSC Mars-1 <sup>a</sup>	MGS-1 <sup>b</sup>	MMS-2 <sup>c</sup>
Crystalline phases	...	65.2	100
Plagioclase feldspar	major component	27.1	77.3
Pyroxene	detected	20.3	8.5
Olivine	detected	13.7	...
Magnetite	detected	1.9	...
Hematite	nano-phase ferric oxide	0.5	3.8
Anhydrite (CaSO <sub>4</sub> 2H <sub>2</sub> )	...	...	6.5
Quartz	...	not detected	1.1
Cristobalite	...	...	2.8
Phyllosilicates	<1	not detected	...
Amorphous phases	majority	34.8	
Basaltic glass	possible	22.9	0.1
Hydrated silica (opal)	...	22.9	...
Mg sulfate	...	4	...
Ferrihydrite	np-Ox	3.5	...
Fe carbonate	...	1.4	...

#### Notes.

<sup>a</sup> Qualitative mineralogy according to Allen et al. (1998).

<sup>b</sup> Semiquantitative (XRD) mineralogy according to Exolith Lab specifications.

<sup>c</sup> Semiquantitative (XRD) mineralogy, this work.

equivalent spheres, i.e., the radius of a sphere that has a projected surface area equal to the projected area of the nonspherical particle averaged over all directions. It is apparent that the S and L size fractions have narrow monomodal size distributions. The M fractions are more problematic. While the JSC Mars-1 M displays a clean monomodal distribution, there is a residual of smaller particles in the MMS-2 M (red squares), and MGS-1 M (gray squares) shows a bimodal size distribution with a significant presence of particles corresponding to MGS-1 S (gray triangles). In the latter case, the scanning electron microscope (SEM) images confirm the presence of S particles attached to M particles (see Section 3.3). Particle-size

**Table 3**  
The Effective Radii and Effective Variances of the Samples

Sample	$r_{\text{eff}}$ ( $\mu\text{m}$ )	$v_{\text{eff}}$
JSC Mars-1 L	16.5	0.09
JSC Mars-1 M	2.7	0.28
JSC Mars-1 S	0.4	0.03
MGS-1 L	17.4	0.12
MGS-1 M	1.6	0.75
MGS-1 S	0.4	0.06
MMS-2 L	16.2	0.12
MMS-2 M	2.3	0.28
MMS-2 S	0.3	0.18

distributions are typically characterized by their effective radii  $r_{\text{eff}}$  and variances  $v_{\text{eff}}$  (Hansen & Travis 1974):

$$r_{\text{eff}} = \frac{\int_0^{\infty} r \pi r^2 n(r) dr}{\int_0^{\infty} \pi r^2 n(r) dr}, \quad (2)$$

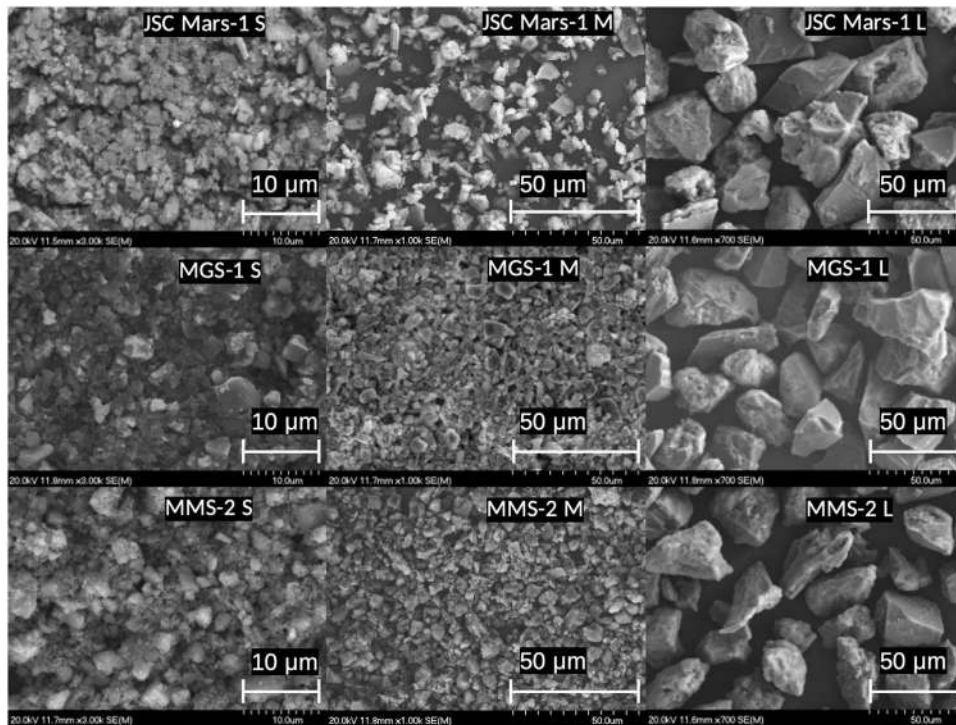
$$v_{\text{eff}} = \frac{\int_0^{\infty} (r - r_{\text{eff}})^2 \pi r^2 n(r) dr}{r_{\text{eff}}^2 \int_0^{\infty} \pi r^2 n(r) dr}. \quad (3)$$

The obtained effective radii ( $r_{\text{eff}}$ ) and effective variances ( $v_{\text{eff}}$ ) of the size fractions are listed in Table 3.

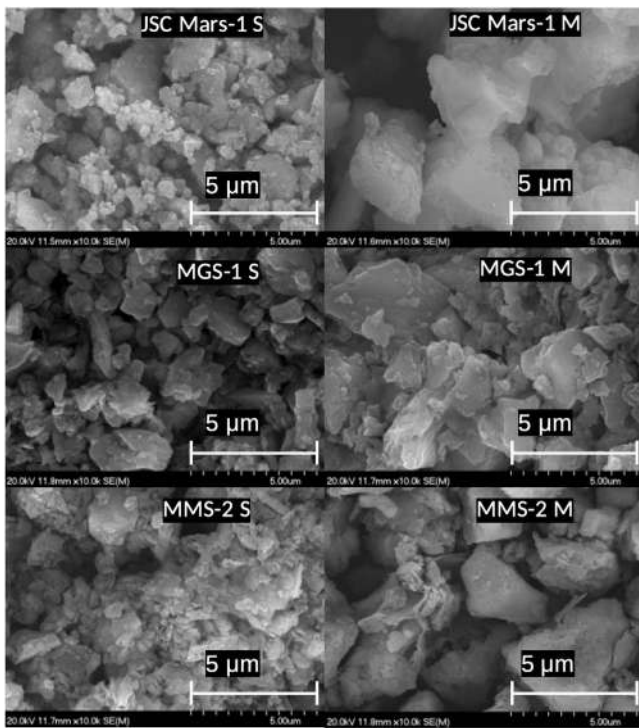
### 3.3. Shapes and Complex Refractive Indices

Figure 3 shows the SEM images of the samples prepared for scattering-matrix measurements. They have been obtained at different magnifications. This provides a detailed view of the properties of the surfaces and structure of the particles as well as additional information about the size of the particles. As an example Figure 4 shows the samples in the first two columns of Figure 3 with a higher magnification, to highlight how the MMS-2 M and MGS-1 M fractions contain S particles, albeit in





**Figure 3.** SEM images of the S, M, and L samples of the three Martian dust simulants JSC Mars-1, MGS-1, and MMS-2. The number at the lower-right corner of the left panels indicates the total length of the scale ruler (horizontal white lines).



**Figure 4.** SEM images of the S and M samples of the three Martian dust simulants JSC Mars-1, MGS-1, and MMS-2 at higher magnification. These images demonstrate the presence of S particles in the M fractions of MGS-1 and MMS-2. The number at the lower-right corner of the left panels indicates the total length of the scale ruler (horizontal white lines).

the latter case the S particles are much more abundant, in agreement with the particle-size distributions in Figure 2. In contrast, the JSC Mars-1 M fraction is completely clean of S particles.

**Table 4**

The Imaginary Parts of the Refractive Indices,  $k$ , for the JSC Mars-1, MGS-1, and MMS-2 Analogs at 488 and 640 nm Interpolated from the Values Obtained by Martikainen et al. (2023)

Sample	$k$ (488 nm)	$k$ (640 nm)
JSC Mars-1	0.00095	0.00065
MGS-1	0.00042	0.00043
MMS-2	0.0011	0.00035

**Note.** The real part of the refractive index,  $n$ , was fixed to 1.5.

**Table 5**

Number of Nonzero Elements of the Scattering Matrices that Have Been Measured for Each Sample

Samples	488 nm			640 nm		
	L	M	S	L	M	S
JSC Mars-1	6	3	2	6	6	2
MGS-1	6	3	2	6	6	2
MMS-2	6	3	2	6	6	2

**Note.** The minimum is two (phase function and degree of linear polarization).

Particle composition is described through the wavelength-dependent complex refractive indices ( $m = n + ik$ ). The real part of the complex refractive index,  $n$ , describes the ratio of the speed of light in a vacuum to the phase velocity of light in the material, and the imaginary part,  $k$ , describes the absorption of light inside the material. The complex refractive indices of the simulants were retrieved by Martikainen et al. (2023) using the measured reflectance spectra, measured particle-size distributions, and an advanced light-scattering model that accounts for the irregular shapes of the dust particles. The derived refractive indices were validated by reproducing the

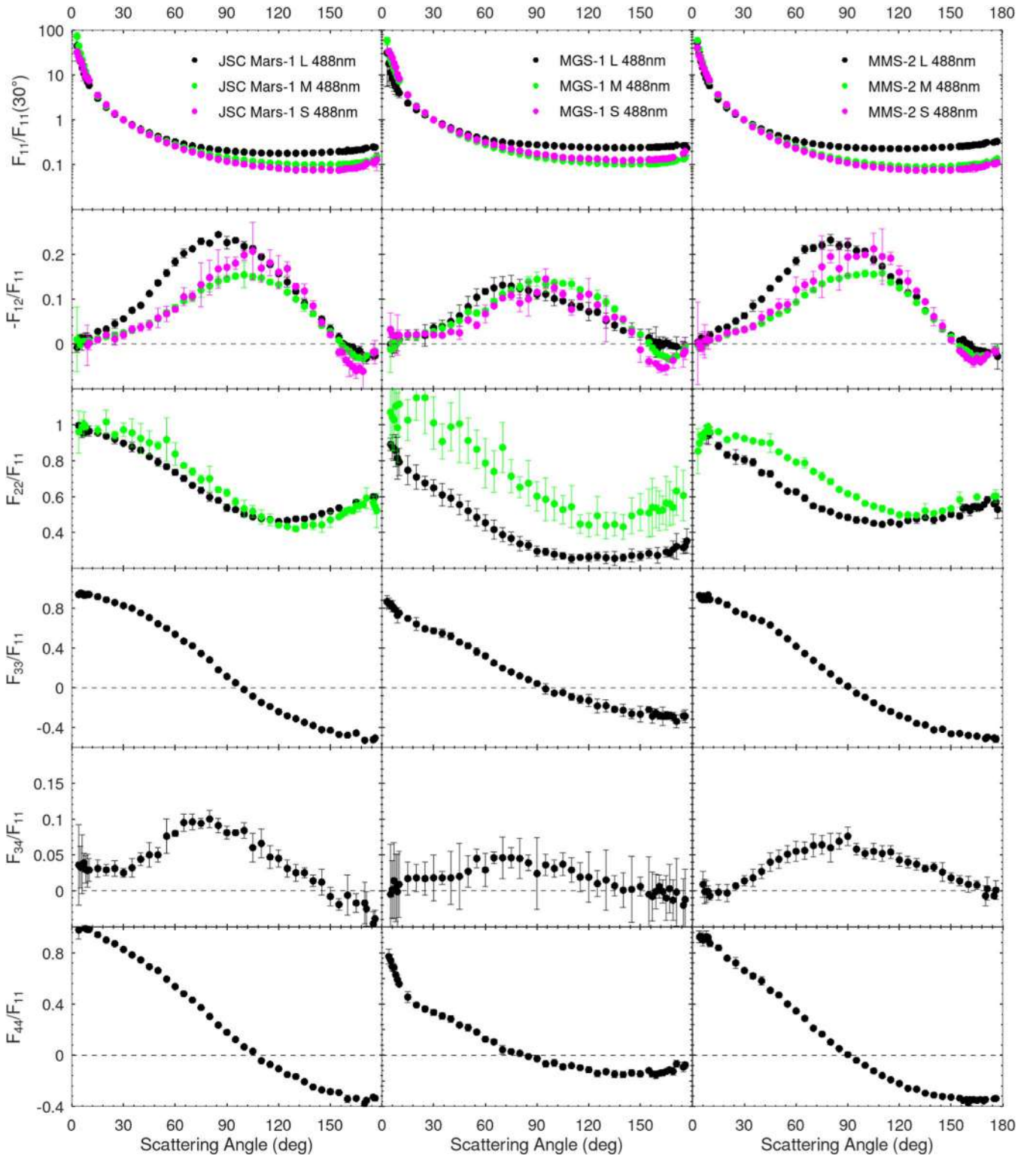


**Figure 5.** Scattering-angle dependence of the normalized scattering-matrix elements  $F_{11}/F_{11}(30^\circ)$ ,  $-F_{12}/F_{11}$ ,  $F_{22}/F_{11}$ ,  $F_{33}/F_{11}$ ,  $F_{34}/F_{11}$ , and  $F_{44}/F_{11}$  at 488 nm of the JSC Mars-1, MGS-1, and MMS-2 Martian dust analogs.

spectrum of the Martian surface observed by the ultraviolet and visible channel of the Nadir and Occultation for Mars Discovery spectrometer on board the ExoMars mission (see Willame et al. 2022). The interpolated values at 488 and 640 nm for each simulant are listed in Table 4. The MMS-2 simulant shows the largest differences in absorption between

488 and 640 nm: it is the darkest analog at 488 nm and the brightest at 640 nm. The reflectance spectrum of the MGS-1 analog is relatively flat and thus does not exhibit high variance in absorption at visible wavelengths. The JSC Mars-1 analog is slightly less absorbing at 488 nm than the MMS-2, however, at 640 nm it is noticeably darker than the other two analogs.



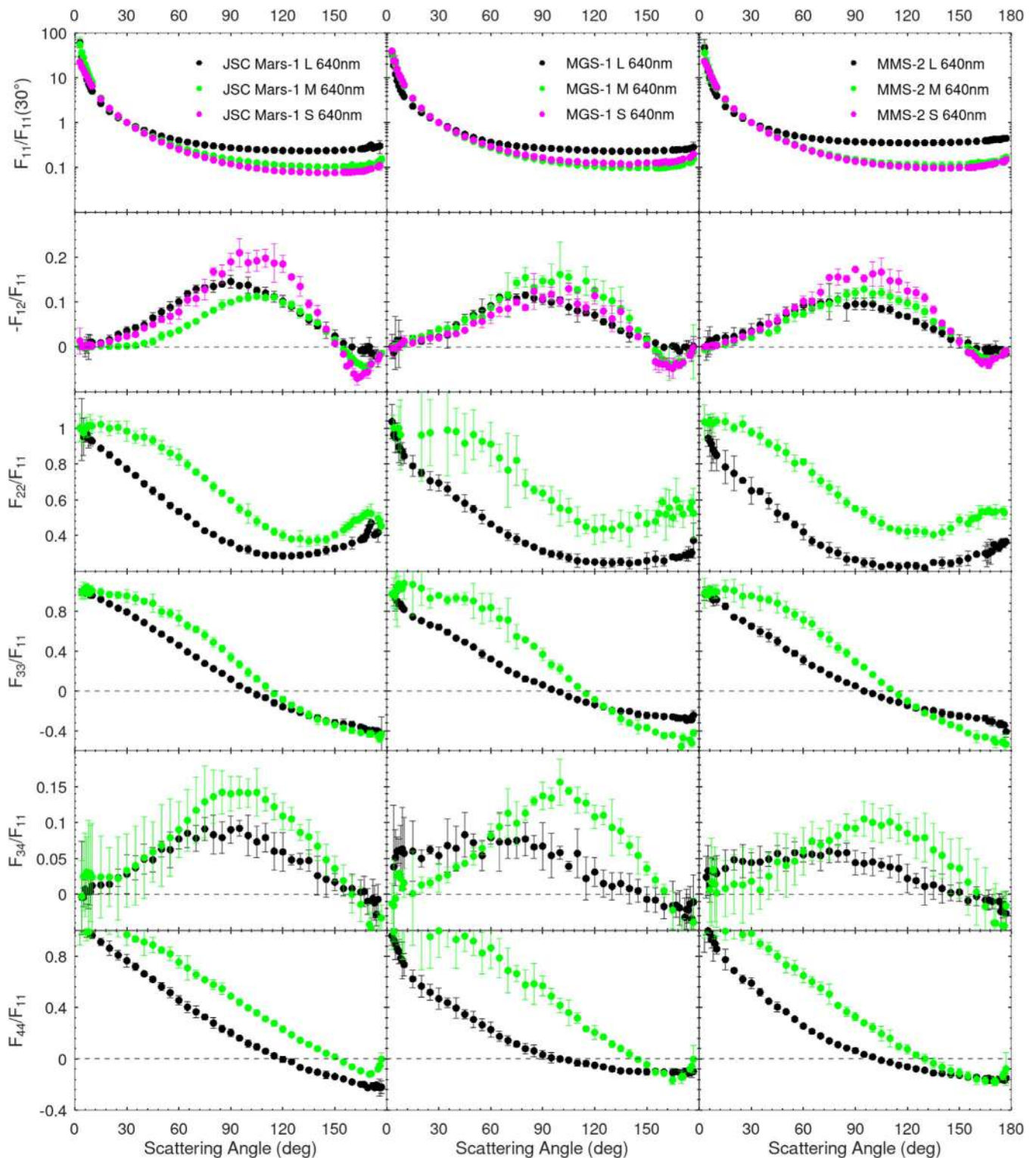


**Figure 6.** Scattering-angle dependence of the normalized scattering-matrix elements  $F_{11}/F_{11}(30^\circ)$ ,  $-F_{12}/F_{11}$ ,  $F_{22}/F_{11}$ ,  $F_{33}/F_{11}$ ,  $F_{34}/F_{11}$ , and  $F_{44}/F_{11}$  at 640 nm of the JSC Mars-1, MGS-1, and MMS-2 Martian dust analogs.

#### 4. Experimental Data

The scattering matrices at 488 and 640 nm of the JSC Mars-1, MGS-1, and MMS-2 for the size fractions L, M, and S have been measured at CODULAB (Muñoz et al. 2011).

The  $F_{11}$  and  $-F_{12}$  are the only two elements that can be measured using passive remote sensing and hence have been measured for all of the samples considered. The rest of the

nonzero elements have been measured for some size fractions (see Table 5), depending on a number of limiting factors, such as the amount of sample available. The elements of the scattering matrices at 488 and 640 nm are plotted as a function of the scattering angle ( $3^\circ < \theta < 177^\circ$ ) in Figures 5 and 6, respectively. We note that samples consisting of particles smaller than  $1\ \mu\text{m}$  tend to stick to each other during the

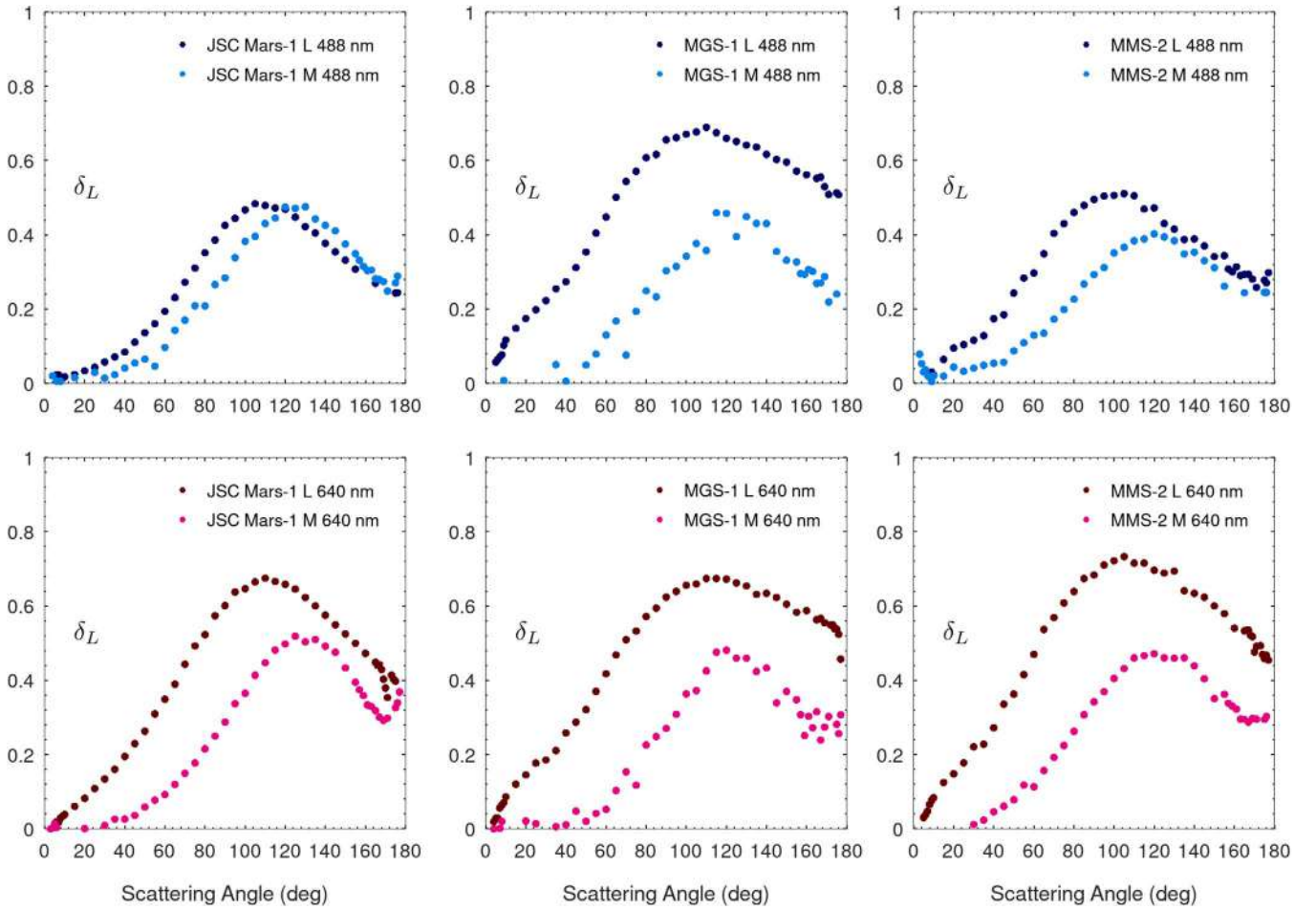


**Figure 7.** The linear depolarization ratios for the JSC Mars-1, MGS-1, and MMS-2 L and M samples at 488 and 640 nm.

**Table 6**  
Parameters Extracted from the Phase Function and  $P$  Curves

Sample	$\lambda$ (nm)	Size	$P_{\min}$	$\theta_{\min}$	$P_{\max}$	$\theta_{\max}$	$\theta_{\text{inv}}$
JSC Mars-1	488	L	$-3.2 \pm 1.2$	$171 \pm 3$	$24.4 \pm 0.4$	$85 \pm 5$	$158 \pm 3$
	488	M	$-4.2 \pm 0.2$	$169 \pm 3$	$15.0 \pm 3.0$	$100 \pm 5$	$156 \pm 3$
	488	S	$-6.0 \pm 4.0$	$169 \pm 3$	$21.0 \pm 6.0$	$105 \pm 5$	$153 \pm 3$
	640	L	$-2.6 \pm 1.8$	$177 \pm 3$	$14.6 \pm 1.4$	$90 \pm 5$	$160 \pm 3$
	640	M	$-4.5 \pm 0.5$	$167 \pm 3$	$11.3 \pm 0.5$	$105 \pm 5$	$154 \pm 3$
	640	S	$-7.0 \pm 1.5$	$163 \pm 3$	$21.0 \pm 3.0$	$95 \pm 5$	$151 \pm 3$
MGS-1	488	L	$-1.0 \pm 1.5$	$177 \pm 3$	$13.1 \pm 1.9$	$70 \pm 5$	$162 \pm 3$
	488	M	$-3.5 \pm 0.3$	$167 \pm 3$	$14.4 \pm 1.6$	$90 \pm 5$	$155 \pm 3$
	488	S	$-4.8 \pm 0.4$	$163 \pm 3$	$15.0 \pm 2.2$	$95 \pm 5$	$150 \pm 3$
	640	L	$-1.0 \pm 1.0$	$169 \pm 3$	$11.6 \pm 0.7$	$80 \pm 5$	$160 \pm 3$
	640	M	$-3.9 \pm 1.4$	$165 \pm 3$	$16.0 \pm 7.0$	$100 \pm 5$	$153 \pm 3$
	640	S	$-4.8 \pm 2.2$	$165 \pm 3$	$13.0 \pm 1.3$	$105 \pm 5$	$150 \pm 3$
MMS-2	488	L	$-2.0 \pm 0.3$	$176 \pm 3$	$23.2 \pm 1.2$	$80 \pm 5$	$161 \pm 3$
	488	M	$-2.8 \pm 0.4$	$167 \pm 3$	$15.8 \pm 1.7$	$110 \pm 5$	$154 \pm 3$
	488	S	$-4.1 \pm 1.1$	$163 \pm 3$	$21.0 \pm 3.0$	$105 \pm 5$	$152 \pm 3$
	640	L	$-1.3 \pm 1.5$	$166 \pm 3$	$10.6 \pm 1.4$	$80 \pm 5$	$160 \pm 3$
	640	M	$-2.8 \pm 0.6$	$169 \pm 3$	$12.9 \pm 1.9$	$95 \pm 5$	$153 \pm 3$
	640	S	$-4.1 \pm 0.8$	$167 \pm 3$	$17.3 \pm 0.4$	$90 \pm 5$	$151 \pm 3$

measurements creating larger aggregates, which is the reason for the high variability measured in the S sample. In general, the measurements for the MGS-1 samples (all size ranges) show larger error bars than the measurements for all the other

samples, even when they were measured under the same experimental conditions. This is primarily due to the limited amount of sample available for conducting the experiments. In the case of the MGS-1 analog, the amount of sample was even



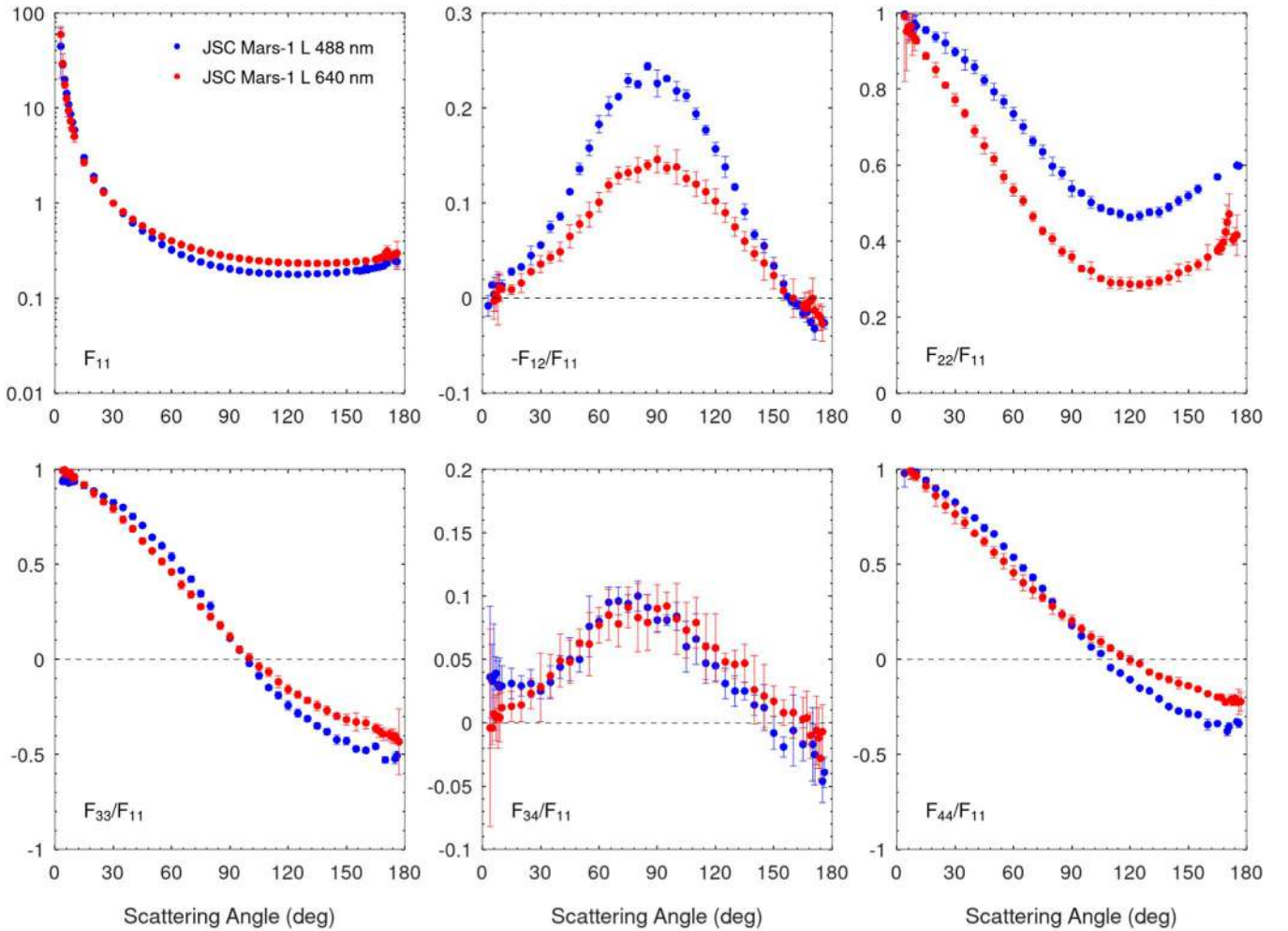


**Figure 8.** The measured scattering-matrix elements of the JSC Mars-1 L analog at 488 and 640 nm.

smaller than that of MMS-2 and JSC Mars-1. When that is the case, fewer particles end up in the scattering volume during the measurements, consequently reducing the signal-to-noise ratio.

Table 6 lists some parameters extracted from the phase function and  $P$  curves plotted in Figures 5 and 6. These parameters are:

1. The minimum value of the  $P$  in the negative polarization branch within the range of measured scattering angles,  $P_{\min}$  (%).
2. The scattering angle corresponding to the minimum value of the  $P$ ,  $\theta_{\min}$ .
3. The maximum value of the  $P$  within the range of measured scattering angles,  $P_{\max}$  (%).
4. The scattering angle corresponding to the maximum value of the  $P$ ,  $\theta_{\max}$ .
5. The scattering angle for which the  $P$  changes sign (i.e., the inversion angle),  $\theta_{\text{inv}}$ .

## 5. Discussion

### 5.1. Size Effect

Many of the parameters in Table 6 show a clear dependence with particle size. All of the measured phase functions show strong forward peaks and flat featureless curves at side and backscattering directions typically observed for irregular dust

particles. The phase functions of the L size fraction are relatively flat at back- and side-scattering angles with a strong increase in the forward direction forming a narrow peak, whereas the M and S size fractions show a broader forward peak that develops into a steeper slope toward the side-scattering direction, finally increasing from its minimum toward the backward direction. The narrower forward peaks for larger particle sizes are consistent with the diffraction theory. In general, the M and S size fractions show similar phase curves, with the M fraction having a curve somewhat flatter than the S fraction. The MGS-1 analog is slightly different with respect to the other analogs as the phase curve of the S size is flatter than for the M size. It is important to note that the measured size distributions of the MGS-1 sample deviate from the other two analogs to some extent.

The  $P$  curves exhibit typical features for irregular dust particles with the characteristic bell shape, a negative polarization branch (NPB) near the backscattering direction, and a maximum at side-scattering angles. We observe that the inversion angle decreases and the maximum of the  $P$  curve shifts toward larger scattering angles with a decreasing particle size. As previously shown by Muñoz et al. (2021), particle size affects the maximum polarization and the depth of the NPB. We notice that the NPB diminishes as the size of the particles increases: the S size fraction exhibits a deep NPB that becomes shallower with increasing particle size. The NPB is weak for the MGS-1 L size, whereas in

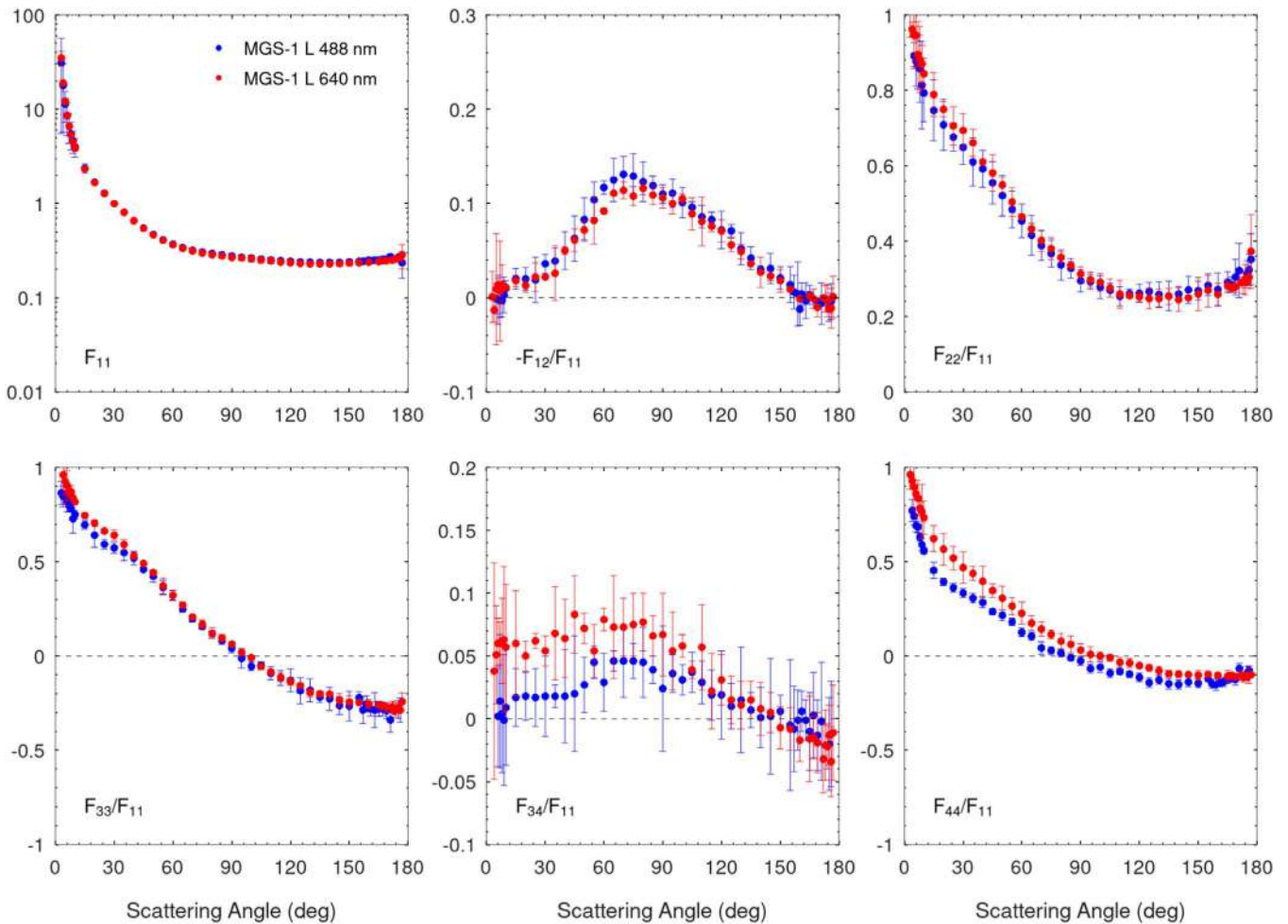


**Figure 9.** The measured scattering-matrix elements of the MGS-1 L analog at 488 and 640 nm.

the cases of the JSC Mars-1 and MMS-2 L size fractions, the NPB is significantly noticeable at 488 nm. This effect can be explained by the constructive interference of light multiply scattered within the particle by wavelength-scale surface roughness and/or internal structure, causing the so-called coherent backscattering mechanism (Shkuratov 1989; Muinonen 1990; Muinonen et al. 2015). The NPB is observable for the JSC Mars-1 and MMS-2 L sizes due to the negative polarization having a strong dependence on material absorption properties (see Muinonen et al. 2007; Zubko et al. 2009, 2015); higher absorption creating a deeper NPB. Our results are in agreement with those of Muñoz et al. (2021). As the measured angle range is limited to  $177^\circ$ , angular features of the NPB at larger scattering angles cannot be discussed further. We note that the  $P$  main features are highly dependent on the particle absorption properties, as will be discussed in the following section.

The  $F_{22}/F_{11}$  element, which is directly related to the linear depolarization ratio used in lidar measurements, shows variations in the measured curves that depend on the particle sizes. In lidar studies, it is important to take into account that  $\delta_L$  is not only linked to the particle shapes and composition, but also to the particle sizes (see, e.g., Kahnert et al. 2020; Saito & Yang 2021; Kong et al. 2022). Retrieving physical and optical properties from lidar data can become challenging as the side- and forward-scattering angles are omitted. In Figure 7, we show the calculated  $\delta_L$  (Equation (1)) for the L and M samples

at 488 and 640 nm. In general, the maximum  $\delta_L$  value shifts toward larger scattering angles with decreasing size. In the case of the JSC Mars-1 analog, the size fractions converge near the backscattering direction making it difficult to distinguish one size from another based on  $\delta_L$ . A similar trend can be observed for the MMS-2 size fractions at 488 nm. Our results are in agreement with those of Muñoz et al. (2021). The changes in  $\delta_L$  values seem to correlate with material absorption properties: higher absorption produces smaller differences near the backscattering direction brushing out the differences caused by the particle size. We note that due to the limitation set by the range of the measurement angles, not much can be said about the exact backscattering angle at  $180^\circ$ .

The measured  $F_{34}/F_{11}$  element displays a flatter curve the larger the particle size is. This trend could be partly caused by the internal structure of the particles and/or wavelength-scale surface roughness that promote multiple scattering within a particle. The effect has been previously studied through light-scattering simulations by Escobar-Cerezo et al. (2017). Similarly, we notice significant differences in the measured  $F_{33}/F_{11}$  and  $F_{44}/F_{11}$  ratios: the L size fraction produces a deeper U-shaped curve that flattens toward the backscattering direction, whereas the curves of the M size start as more flat before steeply decreasing toward the side- and backscattering directions.

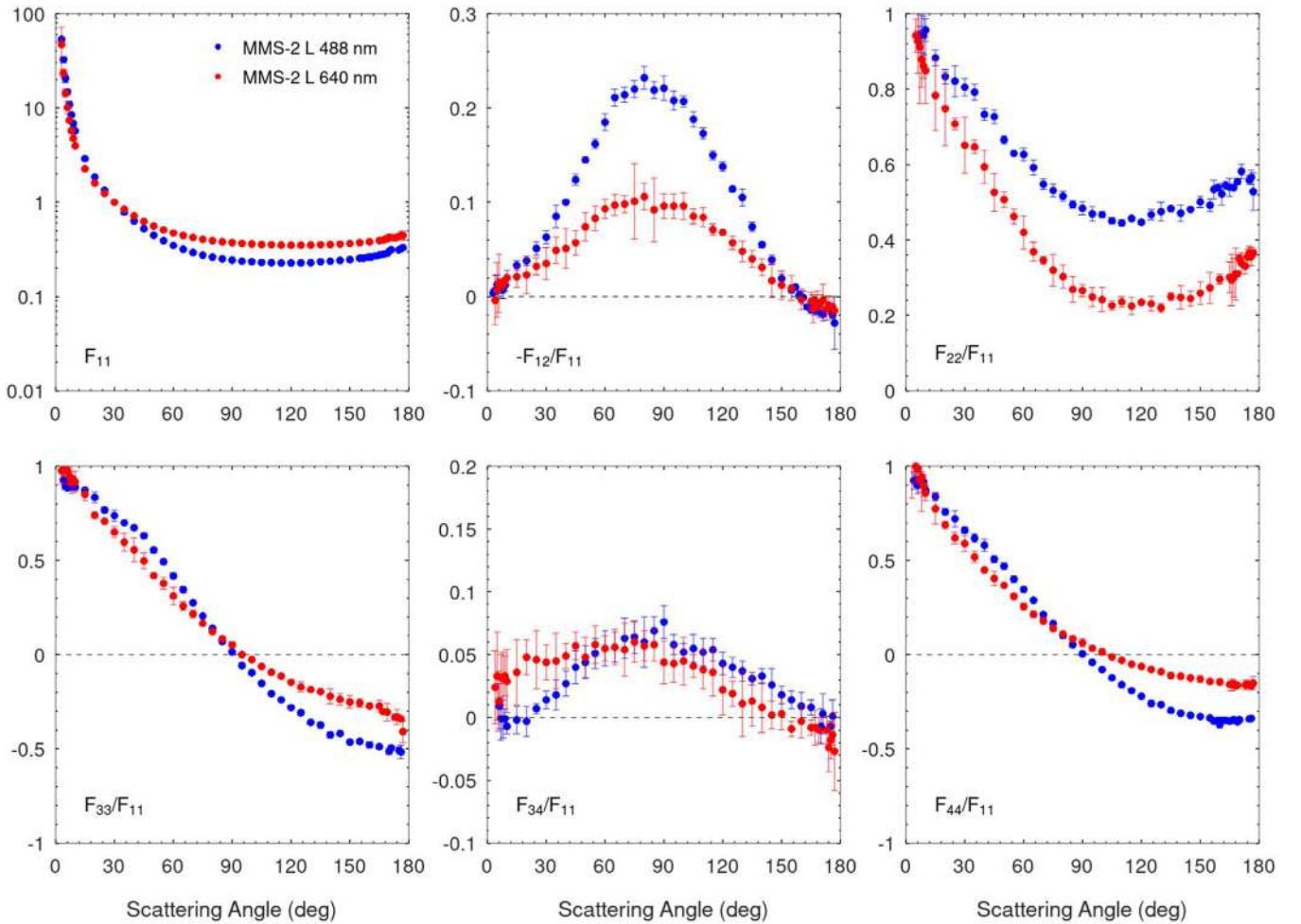


**Figure 10.** The measured scattering-matrix elements of the MMS-2 L analog at 488 and 640 nm.

### 5.2. Composition/Wavelength Effect

The analogs were selected so that they represent a variety of different materials, each of them having their own distinctive spectral features and colors. As shown by Martikainen et al. (2023), all of the samples absorb more light at shorter wavelengths. In Figure 5, we observe that at 488 nm the L size fraction has the highest  $P$  maximum, and the M size fraction the lowest, with an exception of the MGS-1 analog that shows similar maximum values. The differences become more evident the more absorption there is in the material. At 640 nm (Figure 6), the S size fraction displays the highest  $P$  maximum for the JSC Mars-1 and MMS-2 simulants, whereas the MGS-1 shows similar behavior in blue and red. A change in the refractive index affects the L size fraction the most due to light traveling longer inside the absorbing medium, and thus larger differences can be observed in the maxima of the  $P$  curves of the L samples between different wavelengths.

When comparing different wavelengths, changes in both absorption and apparent size have an effect. Figures 8–10 show the wavelength dependence for the full scattering matrices of the L samples. The phase function becomes flatter at side- and backscattering directions, and the maximum of the  $P$  curve decreases and shifts slightly toward larger scattering angles when changing from blue to red. As MMS-2 is the darkest simulant at 488 nm and the brightest at 640 nm, it displays the most prominent differences. According to Table 4, the MGS-1

analog shows little change in the refractive indices at the measured wavelengths, thus explaining why the measured scattering matrices in both blue and red are similar.

It is of high interest to see the transformation of the wavelength dependence of the phase curve and polarization maximum with changing particle size. In Figures 11 and 12, we show the wavelength effect on the phase functions and  $P$  curves of the M and S samples. With a decreasing size, the differences become less prominent. Similarly to the changes that could be seen for the L size, the JSC Mars-1 and MMS-2 M samples show flatter phase functions at side- and backscattering directions, whereas the maxima of the  $P$  curves decrease and shift slightly toward larger scattering angles when going from blue to red light. Again, the MGS-1 M sample shows little change in the measured scattering matrices due to the similar values of complex refractive indices at the two wavelengths. In the case of the S samples, one must be careful when interpreting the measurement data. Very small particles tend to stick together during the measurements forming aggregates and causing large measurement errors. In Figure 12, noticeable changes in the measured phase functions and  $P$  curves cannot be observed for the JSC Mars-1 and MGS-1 S sizes. However, the MMS-2 S sample that has the largest difference in its absorption properties between the blue and red wavelengths shows a similar trend to what was seen for the L and M sizes: a flatter phase function at side- and backscattering directions, and a decrease in the



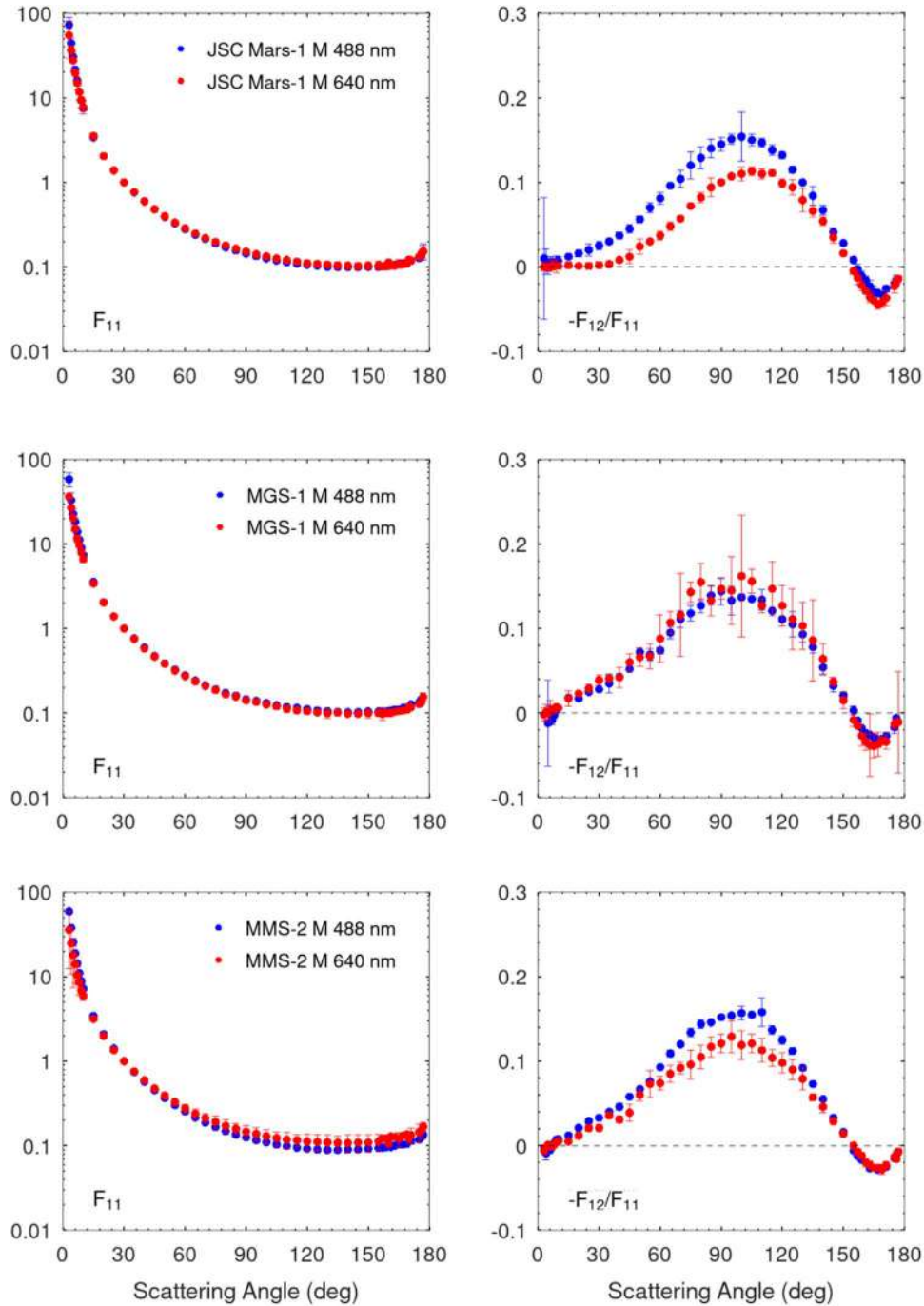


**Figure 11.** The measured phase functions and  $P$  curves of the JSC Mars-1, MGS-1, and MMS-2 M sizes at 488 and 640 nm.

maximum of the  $P$  curve when changing from blue to red. The maximum of the  $P$  does not show any noticeable shift.

In Figures 13 and 14, we compare the measured scattering matrices of the three analogs for the L size fraction at 488 and 640 nm, respectively. At 488 nm, MGS-1 is the least absorbing simulat, which can be clearly seen as a noticeably lower  $P$  maximum when compared to the other two samples. Furthermore, the  $F_{22}/F_{11}$  element, and therefore also  $\delta_L$ , is sensitive to the differences in the refractive indices exhibiting a significantly lower curve for the MGS-1 analog. As lidar measurements are carried out at the backscattering direction, we emphasize that making a distinction between the JSC Mars-1 and MMS-2 analogs is challenging without taking into account

the side- and forward-scattering directions (see Figure 7). Small differences can be observed in the other scattering-matrix elements. Due to the MMS-2 analog being only slightly more absorbing in blue than the JSC Mars-1, the differences in their scattering matrices are smaller. Surprisingly, all of the scattering-matrix elements of the MMS-2 are somewhere in between the JSC Mars-1 and MGS-1 analogs, which could be related to differences in the real parts of the refractive indices. At 640 nm, the differences between the measured scattering-matrix elements are less evident (excluding the phase function) as the complex refractive indices of the samples do not differ profusely. The JSC Mars-1 analog, being the darkest, has a somewhat larger maximum of the  $P$  curve and a slightly higher

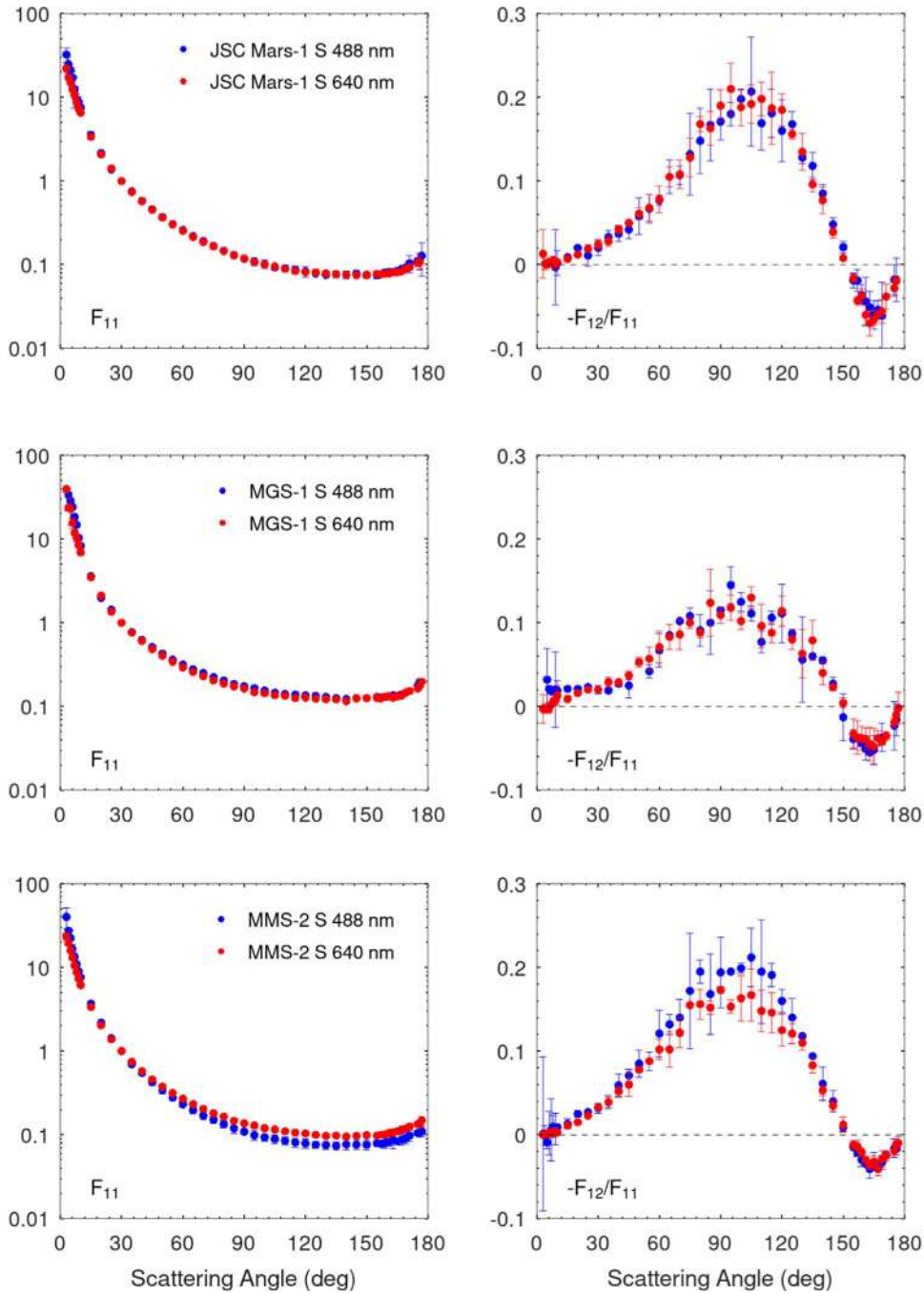


**Figure 12.** The measured phase functions and  $P$  curves of the JSC Mars-1, MGS-1, and MMS-2 S sizes at 488 and 640 nm.

$F_{22}/F_{11}$  curve, whereas the MMS-2 analog, being the brightest, has a more flat phase-function curve in the side- and backscattering angles. The location of the  $P$  maximum shifts toward larger scattering angles the more absorbing the analog is. Our measurements further confirm (see e.g., Muñoz et al. 2021) that the forward peak of the phase function is mainly dependent on the particle size (larger particles produce a narrower peak), whereas at side- and backscattering angles both composition and size have an effect.

## 6. Comparison with Observations

Observed sky-brightness curves of the Martian atmosphere give us clues about dust-grain sizes, shapes, and compositions

during different dust conditions. A previous study by Chen-Chen et al. (2019a) compared the observed sky-brightness curves to the measured phase function of a basalt sample studied by Dabrowska et al. (2015) and further carried out radiative-transfer modeling to obtain modeled sky brightnesses. The results indicated that the shapes of the phase functions measured in a laboratory can be roughly compared to the shapes of the observed sky-brightness curves as features of the modeled sky brightness do not differ significantly from the measured phase function used in the model.

Here, we compare the measured phase functions of the JSC Mars-1, MMS-2, and MGS-1 analogs to sky-brightness curves observed during different states of the atmosphere (see Figure 15). The observations were carried out using the

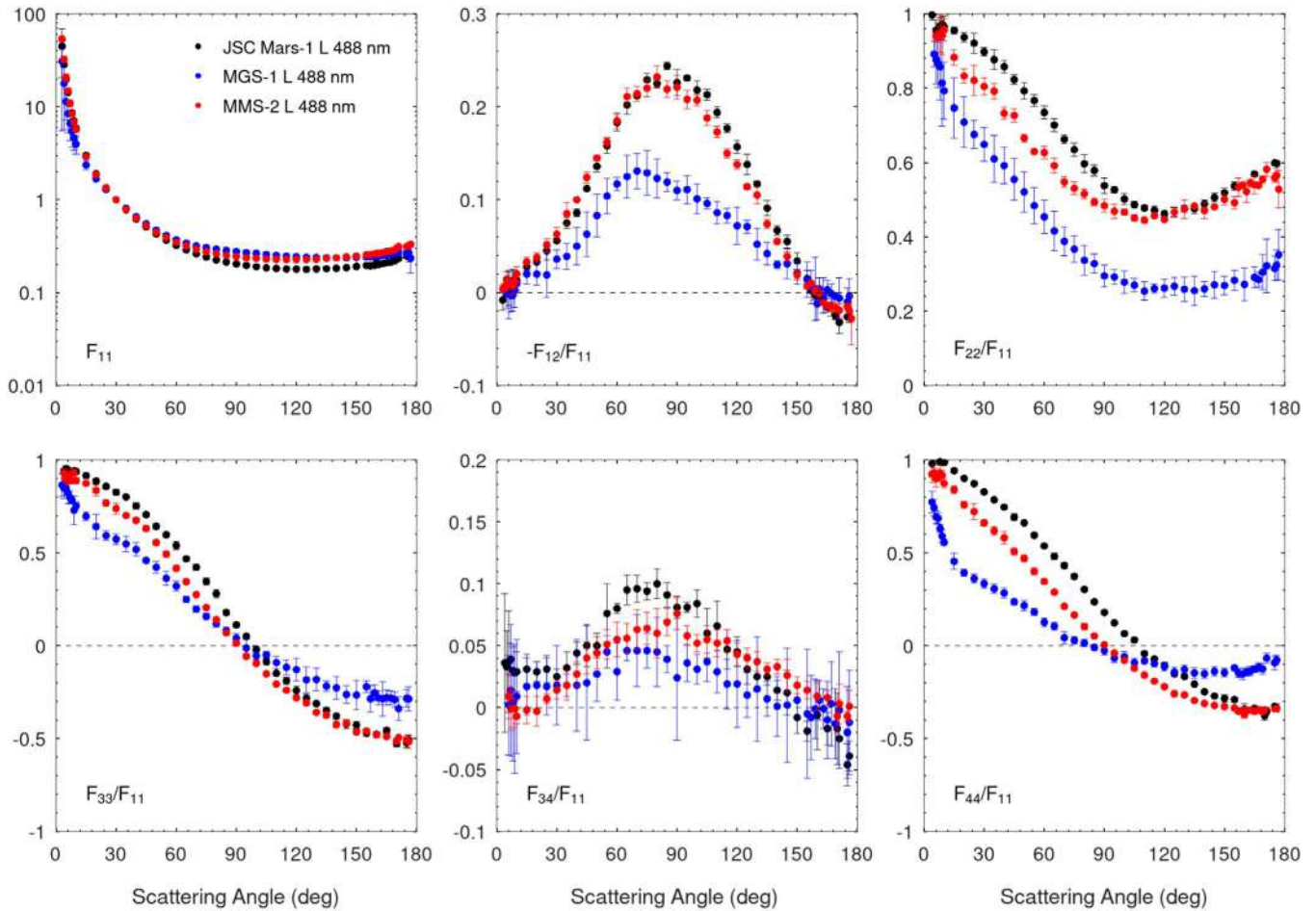


**Figure 13.** The measured scattering-matrix elements of the JSC Mars-1, MGS-1, and MMS-2 L samples at 488 nm.

Navcam and Hazcam engineering cameras on board the MSL rover (see Maki et al. 2012) with an effective wavelength of 650 nm and have been published by Chen-Chen et al. (2019b). The Navcam absolute radiance uncertainty is estimated to be about 12%, while the Hazcam absolute radiance uncertainty is about 17% (Chen-Chen et al. 2019a). Sky-brightness curves for two dust conditions were observed:

1. Sol 1258 (Ls 111°) that corresponds to the normal state of the atmosphere ( $\tau_{\text{dust}} = 0.5$ ).
2. Sol 1581 (Ls 300°) with a dusty atmosphere ( $\tau_{\text{dust}} = 0.8$ ).

We have normalized the observed sky-brightness curves to 1 at 30° in order to perform a comparison with the normalized measured phase functions. The phase functions of the L size distributions show a narrower peak in the forward direction with a flatter curve toward larger scattering angles when compared to the smaller particle sizes. A similar effect can be seen for the observed sky-brightness curves with an increasing  $\tau_{\text{dust}}$ . In the case of the analogs, the flattening of the curve can be partly caused by the increase of multiple scattering within a single particle caused by the interactions of electromagnetic waves with internal structure and small-scale geometric boundaries at the particle’s surface as shown by Escobar-Cerezo et al. (2017). Likewise, the changes seen in the observed sky brightnesses could be partly explained by an increase in multiple scattering: dust grains in highly dusty conditions are more densely packed encouraging multiple

scattering among particles. Moreover, small particles can aggregate forming larger particles during dusty seasons. From optical images of the Martian sky taken by several surface lander and rover missions, models of sunlight scattering have allowed estimates of the effective radius,  $r_{\text{eff}}$ , of the Martian atmospheric dust. This has yielded an expected  $r_{\text{eff}}$  of around 1.4–1.7  $\mu\text{m}$  (with  $v_{\text{eff}} = 0.2\text{--}0.5$ ), increasing under stormy conditions, reaching values as high as 3–7  $\mu\text{m}$  during the 2018 dust storm (e.g., Chen-Chen et al. 2019a; Lemmon et al. 2019) suggesting particle aggregation and/or larger particles being lifted and suspended in the air. These values, however, represent an average over the vertical column, i.e., they were derived assuming one single size distribution for all altitudes. Little is known of the vertical distribution of the dust-grain size.

It is difficult to depict which analog samples and size distributions are the most suitable for Martian aerosol studies based on the sky-brightness curves alone as they depend on the composition, shapes, and sizes of the dust grains introducing multiple free parameters to take into consideration. Furthermore, the atmosphere must satisfy  $\tau_{\text{dust}} \ll 1$  for the single-scattering approximation to be applicable. A proper comparison between the observed sky brightnesses and the phase curves measured in a laboratory requires a radiative-transfer treatment to account for possible multiple scattering and atmospheric effects as presented in Chen-Chen et al. (2019a). In general, it is advisable to use larger particle sizes during high dust content, whereas in low dust conditions medium and small sizes are



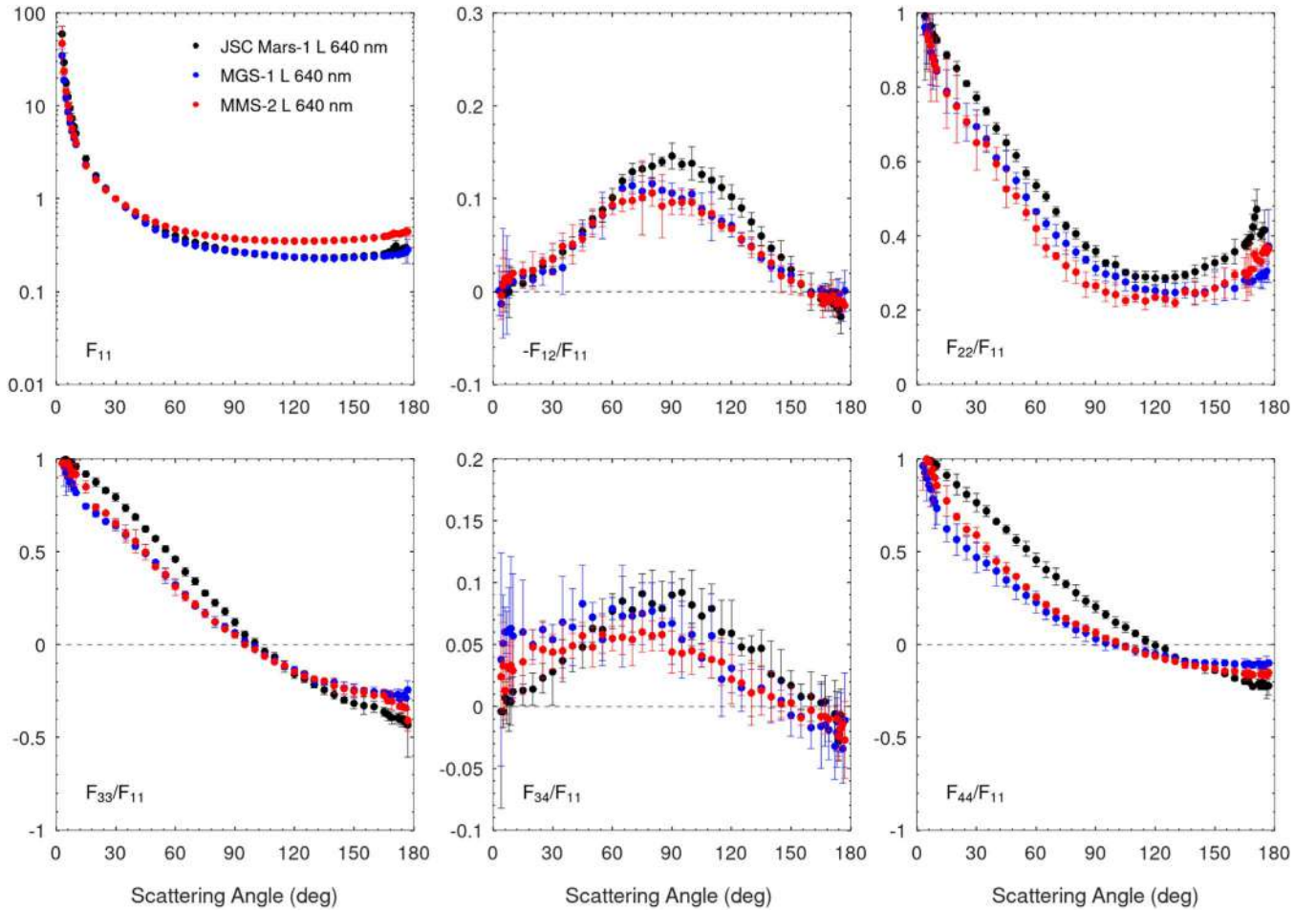


**Figure 14.** The measured scattering-matrix elements of the JSC Mars-1, MGS-1, and MMS-2 L samples at 640 nm.

more dominant. In future studies, polarimetric and spectroscopic observations become crucial as they can provide more insight into the dust found in the Martian atmosphere.

## 7. Conclusions

Full scattering-matrix measurements were carried out for the JSC Mars-1, MGS-1, and MMS-2 Martian dust analogs at 488 and 640 nm. The samples were well characterized with L, M, and S narrow particle-size distributions. Our results are summarized below.

We found that the minimum of the NPB, the position and maximum of the  $P$  curve, and the inversion angle depend on both the size and composition of the particles. The NPB becomes less evident with increasing grain size and the inversion angle shifts to larger scattering angles. At 488 nm, the maximum of the  $P$  curve decreases from the L to the M size fraction but increases for the S size fraction, whereas at 640 nm the S size fraction shows the highest polarization maxima for the JSC Mars-1 and MMS-2 samples that decreases with increasing grain size. The MGS-1 sample differs from the other two analogs showing similar  $P$  maximum values for all sizes. In all of the cases, the  $P$  maximum shifts toward larger scattering angles with decreasing particle size. Furthermore, at 488 nm the analogs display higher maxima of the  $P$  due to increasing absorption within the materials at shorter wavelengths.

All of the measured phase functions show typical behavior of micrometer-sized irregular compact dust particles in random

orientation: strong peaks at the forward direction and a nearly flat featureless curve at side-scattering angles until a soft increase toward the backscattering angles. The forward peak is mainly dependent on the particle size as larger particles create a narrower peak. The side- and backscattering directions are affected by both particle size and composition so that an increase in particle size and a decrease in absorption produce a flatter curve.

We observed that the  $F_{22}/F_{11}$  ratio depends on the material composition and particle size. The more absorption there is the shallower the curve is, while increasing particle size produces a deeper curve. We found that in some cases it is difficult to distinguish different analogs and sizes from each other by using only the linear depolarization ratio at the backscattering direction. This is important to take into account in future lidar studies.

The measured  $F_{34}/F_{11}$  element was found to be flatter for larger particles. A possible explanation could be internal structure of the grains and/or wavelength-scale surface roughness that introduce multiple scattering within the particle.

Finally, we compared observed sky-brightness curves of the Martian atmosphere to the measured phase functions of the analogs. We found that the sky-brightness curves produce a narrower peak at the forward direction and a flatter curve toward the side-scattering direction with an increasing dust load in the atmosphere. A similar effect was observed for the measured phase functions of the dust analogs with increasing

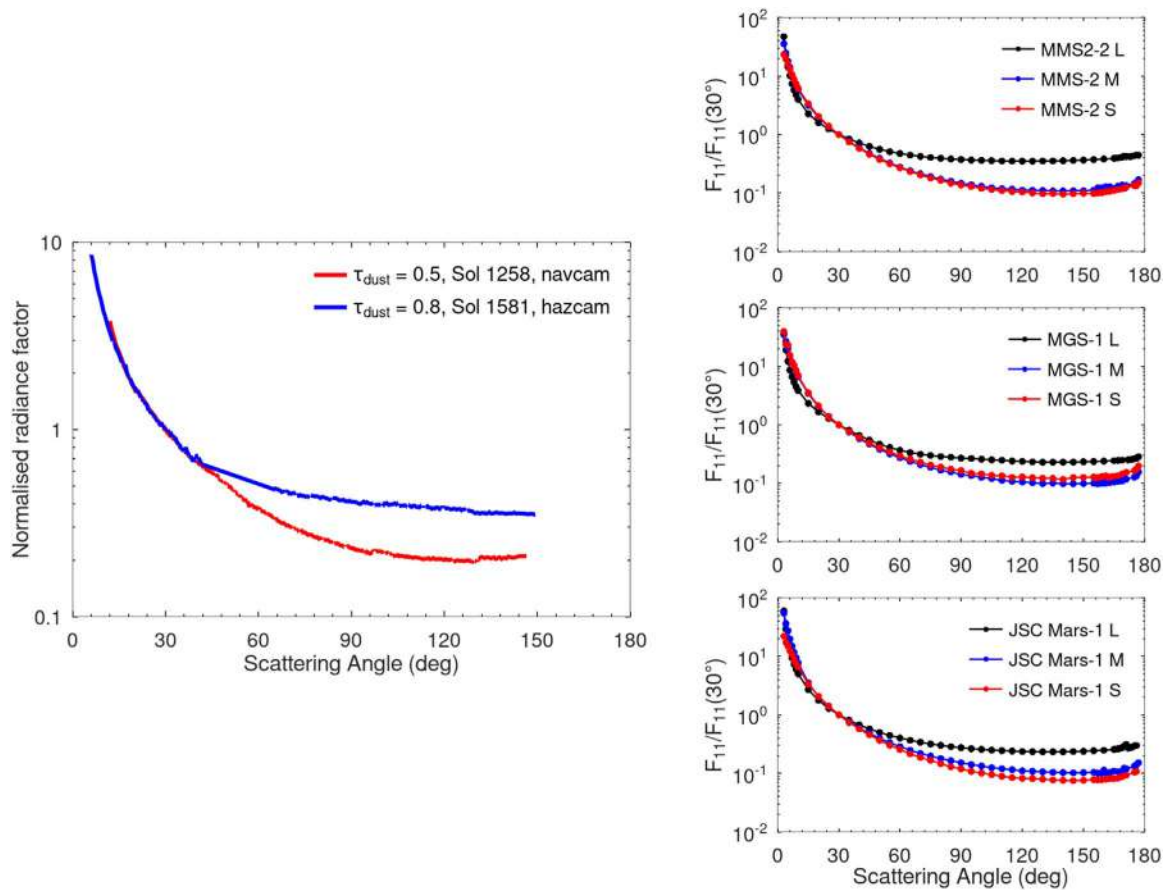


**Figure 15.** The observed sky-brightness curves during different atmospheric dust conditions (left panel) at 650 nm.  $\tau = 0.5$  corresponds to the normal state of the atmosphere, and  $\tau = 0.8$  was obtained during a higher optical depth. The right panels show the measured phase functions of the JSC Mars-1, MMS-2, and MGS-1 analogs for L, M, and S size fractions at 640 nm.

particle size. For the analogs, the flattening of the curve can be caused by an increase in multiple scattering within a particle due to wavelength-scale surface roughness and/or internal inclusions. In the case of the observed sky brightnesses, particle aggregation and multiple scattering among particles in denser dust conditions play a key role.

### Acknowledgments

This work was supported by the European Union’s Horizon 2020 research and innovation program (grant agreement No. 101004052). Research by J.M., O.M., J.C.G.M., and M.P. has been partially supported by PID2021-123370OB-I00/AEI/10.13039/501100011033/FEDER and Severo Ochoa grant CEX2021-001131-S funded by MCIN/AEI/10.13039/501100011033. S.P. H. and A.S.L. have been supported by PID2019-109467GB-I00 (MINECO/FEDER, UE), Elkartek23/09 KK-2023/00077 and Grupos Gobierno Vasco IT-1742-22.

### Data Availability

The experimental scattering-matrix elements as functions of the scattering angle, size distribution tables, and SEM images are freely available at the Granada–Amsterdam light-scattering database (<https://scattering.iaa.es/>) under the request of citation of this paper and the database.

### ORCID iDs

Julia Martikainen <https://orcid.org/0000-0003-2211-4001>  
 Olga Muñoz <https://orcid.org/0000-0002-5138-3932>  
 Juan Carlos Gómez Martín <https://orcid.org/0000-0001-7972-085X>  
 Teresa Jardiel <https://orcid.org/0000-0002-0163-7324>  
 Marco Peiteado <https://orcid.org/0000-0003-3510-6676>  
 Amador C. Caballero <https://orcid.org/0000-0002-0571-6302>  
 Santiago Pérez-Hoyos <https://orcid.org/0000-0002-2587-4682>  
 Agustín Sánchez Lavega <https://orcid.org/0000-0001-7234-7634>  
 Tim Becker <https://orcid.org/0009-0005-2072-4801>  
 Gerhard Wurm <https://orcid.org/0000-0002-7962-4961>  
 Yannick Willame <https://orcid.org/0000-0001-7813-4605>  
 Ann Carine Vandaele <https://orcid.org/0000-0001-8940-9301>

### References

- Allen, C. C., Morris, R. V., Jager, K. M., et al. 1998, *LPSC*, **29**, 1690  
 Amzajerdian, F., Busch, G. E., Edwards, W. C., Cianciolo, A. D., & Munk, M. M. 2012, LPI Contributions 1683, Int. Workshop on Instrumentation for Planetary Missions, ed. LPI Editorial Board, 1092  
 Cannon, K. M., Britt, D. T., Smith, T. M., Fritsche, R. F., & Batchelder, D. 2019, *Icar*, **317**, 470  
 Chen-Chen, H., Pérez-Hoyos, S., & Sánchez-Lavega, A. 2019a, *Icar*, **330**, 16

- Chen-Chen, H., Pérez-Hoyos, S., & Sánchez-Lavega, A. 2019b, *Icar*, **319**, 43
- Chen-Chen, H., Pérez-Hoyos, S., & Sánchez-Lavega, A. 2021, *Icar*, **354**, 114021
- Cremons, D. R., Abshire, J. B., Sun, X., et al. 2020, *CEAS*, **12**, 149
- Dabrowska, D. D., Muñoz, O., Moreno, F., et al. 2015, *Icar*, **250**, 83
- Escobar-Cerezo, J., Palmer, C., Muñoz, O., et al. 2017, *ApJ*, **838**, 74
- Fedorova, A. A., Montmessin, F., Rodin, A. V., et al. 2014, *Icar*, **231**, 239
- Haberle, R., Clancy, R., Forget, F., Smith, M., & Zurek, R. 2017, *The Atmosphere and Climate of Mars* (Cambridge: Cambridge Univ. Press)
- Hansen, J. E., & Travis, L. D. 1974, *SSRv*, **16**, 527
- Hovenier, J. W., Van Der Mee, C., & Domke, H. 2004, *Transfer of Polarized Light in Planetary Atmospheres* (Dordrecht: Kluwer)
- Kahnert, M., Kanngießer, F., Järvinen, E., & Schnaiter, M. 2020, *JSRST*, **254**, 107177
- Kemmerer, B. W. 2019, PhD thesis, Florida Institute of Technology
- Kong, S., Sato, K., & Bi, L. 2022, *JGRD*, **127**, e2021JD035629
- Lemmon, M. T., Guzewich, S. D., McConnochie, T., et al. 2019, *GeoRL*, **46**, 9448
- Lemmon, M. T., Wolff, M. J., Bell, J. F., et al. 2015, *Icar*, **251**, 96
- Maki, J., Thiessen, D., Pourangi, A., et al. 2012, *SSRv*, **170**, 77
- Martikainen, J., Muñoz, O., Jardiel, T., et al. 2023, *ApJS*, **268**, 47
- Min, M., Hovenier, J. W., & de Koter, A. 2003, *A&A*, **404**, 35
- Mishchenko, M. I., Geogdzhayev, I. V., Liu, L., et al. 2003, *JSRST*, **79**, 953
- Mishchenko, M. I., & Hovenier, J. W. 1995, *OptL*, **20**, 1356
- Mishchenko, M. I., Travis, L. D., & Lacis, A. A. 2002, *Scattering, Absorption, and Emission of Light by Small Particles* (Cambridge: Cambridge Univ. Press)
- Modak, A., Sheel, V., & Montmessin, F. 2019, *JESS*, **128**, 144
- Moreno, F., Muñoz, O., Guirado, D., & Vilaplana, R. 2007, *JSRST*, **106**, 348
- Moreno, F., Muñoz, O., López-Moreno, J. J., Molina, A., & Ortiz, J. L. 2002, *Icar*, **156**, 474
- Muironen, K. 1990, PhD thesis, Observatory and Astrophysics Laboratory, Univ. of Helsinki
- Muironen, K., Penttilä, A., & Videen, G. 2015, in *Polarimetry of Stars and Planetary Systems*, ed. L. Kolokolova, J. Hough, & A.-C. Levasseur-Regourd (Cambridge: Cambridge Univ. Press), 114
- Muironen, K., Zubko, E., Tyynelä, J., Shkuratov, Y. G., & Videen, G. 2007, *JSRST*, **106**, 360
- Muñoz, O., Frattin, E., Jardiel, T., et al. 2021, *ApJS*, **256**, 17
- Muñoz, O., Moreno, F., Guirado, D., et al. 2010, *JSRST*, **111**, 187
- Muñoz, O., Moreno, F., Guirado, D., et al. 2011, *Icar*, **211**, 894
- Nousiainen, T. 2009, *JSRST*, **110**, 1261
- Peters, G. H., Abbey, W., Bearman, G. H., et al. 2008, *Icar*, **197**, 470
- Saito, M., & Yang, P. 2021, *GeoRL*, **48**, e2021GL095121
- Shkuratov, I. G. 1989, *AVest*, **23**, 176
- Smith, P. H., Tamppari, L. K., Arvidson, R. E., et al. 2009, *Sci*, **325**, 58
- Stam, D. M., & Hovenier, J. W. 2005, *A&A*, **444**, 275
- Whiteway, J., Daly, M., Carswell, A., et al. 2008, *JGRE*, **113**, E00A08
- Whiteway, J. A., Komguem, L., Dickinson, C., et al. 2009, *Sci*, **325**, 68
- Willame, Y., Depiesse, C., Mason, J. P., et al. 2022, *P&SS*, **218**, 105504
- Zubko, E., Kimura, H., Shkuratov, Y., et al. 2009, *JSRST*, **110**, 1741
- Zubko, E., Muironen, K., Muñoz, O., et al. 2013, *JSRST*, **131**, 175
- Zubko, E., Shkuratov, Y., & Videen, G. 2015, *JSRST*, **150**, 42